NASA/TM—1999-209479

TMI Rain Rate Estimation Over Land and Ocean Utilizing Convective and Stratiform Discrimination

C. Prabhakara, Goddard Space Flight Center, Greenbelt, MD
R. Iacovazzi Jr., Raytheon ITSS Corp., Greenbelt, MD
J.A. Weinman, Goddard Space Flight Center, Greenbelt, MD
G. Dalu, CNR, Cagliari, Italy

National Aeronautics and
Space Administration

Goddard Space Flight Center
Greenbelt, Maryland 20771

September 1999

Available from:

NASA Center for AeroSpace Information
7121 Standard Drive
Hanover, MD 21076-1320
Price Code: A17

National Technical Information Service
5285 Port Royal Road
Springfield, VA 22161
Price Code: A10

ABSTRACT

Tropical Rainfall Measuring Mission (TRMM) Microwave Imager (TMI) radiometer brightness temperature data in the 85 GHz channel (T85) reveal distinct local minima in a regional map containing a Mesoscale Convective System (MCS). This is because of relatively small footprint size (~ 5.5 km) and strong extinction properties in this channel of the TMI. A map of rain rate for that region, deduced from simultaneous measurements made by the Precipitation Radar (PR) on board the TRMM satellite, reveals that these T85 minima, produced by scattering, correspond to local PR rain maxima. Utilizing the PR rain rate map as a guide, we infer from TMI data the presence of three different kinds of thunderstorms or Cbs. They are young, mature, and decaying Cbs that have a scale of about 20 km on the average. Two parameters enable us to infer these three kinds of Cbs objectively: a) the magnitude of scattering depression deduced from local T85 minima and b) the mean horizontal gradient of T85 around such minima. Knowing the category of a given Cb, we can estimate the rain rate associated with it. Such estimation is done with the help of relationships linking T85 minimum to rain rate in each Cb type. Similarly, a weak background rain rate in all the areas where T85 is less than 260 K is deduced with another relationship linking T85 to rain rate. In our rain retrieval model, this background rain constitutes the stratiform rain where the Cbs are absent. Initially, these relationships are optimized or tuned utilizing the PR and TMI data of a few MCS events. After such tuning, the model is applied to independent MCS cases. The areal distribution of light (1–10 mmhr^{-1}), moderate (10–20 mmhr^{-1}), and intense ($\geq$ 20 mmhr^{-1}) rain rates are retrieved satisfactorally. Accuracy in the estimates of the light, moderate and intense rain areas and the mean rain rates associated with such areas in these independent MCS cases is on the average about 15%. Taking advantage of this ability of our retrieval method, one could derive the latent heat input into the atmosphere over the 760 km wide swath of the TMI radiometer in the tropics.

CONTENTS

FIGURES

TABLES

1. INTRODUCTION

Several microwave radiative-transfer rain retrieval models (e.g., Wu and Weinman, 1984; Kummerow et al., 1989; Smith and Mugnai, 1992; and Prabhakara et al., 1995) have taken into consideration microwave scattering by dense solid ice particles, which are generally associated with convective clouds. However, Schols et al. (1999) indicate that in order to explain satellite-borne Special Sensor Microwave Imager (SSM/I)[1] brightness temperature data associated with stratiform precipitation produced by nimbostratus clouds, radiative properties of frozen and melting ice aggregates (snow) with low density have to be considered. Otherwise, a significant uncertainty in estimation of such stratiform rain rates from SSM/I data will result. In order to objectively sense dense ice particles (frozen rain drops and graupel) or less dense ice particles (frozen and melting ice aggregates), a spectral signature is needed from the microwave radiometer data. Such a distinct signature is missing in the limited information contained in the dual-polarization, multispectral SSM/I data (Schols et al., 1995; Prabhakara et al., 1998). This is because measurements in all the channels of this instrument have a high degree of redundancy. In the appendix, we demonstrate this point with measurements made by the Tropical Rainfall Measuring Mission (TRMM)[2] Microwave Imager (TMI) radiometer. This lack of information in the microwave radiometer data can lead to significant errors in rain retrievals that are based solely on radiative transfer theory.

This problem associated with retrieving rain using microwave radiative transfer models is exemplified over oceanic regions by the studies of Heymsfield et al. (1996) and McGaughey and Zipser (1996). They find from aircraft radar and microwave radiometer observations that retrievals from current models that consider dense ice particles perform poorly. Based on the Schols et al. (1999) study, we infer that this is largely due to improper specification of the nature of the ice particles in the models. We may remark that the spatial resolution of these aircraft instruments is a few kilometers, which is much smaller compared to that of the SSM/I. Crude spatial resolution of the satellite borne microwave radiometers is often cited as the dominant reason for significant errors in rain retrievals (e.g., Kummerow, 1998). However, we contend, based on the errors in rain rate retrievals from SSM/I and aircraft radiometer data, that spatial resolution is not the only cause of such errors. The ability to discriminate the nature of ice hydrometeors is also an important factor.

On land regions, rain retrieval from microwave radiometer data is further complicated by variable surface emissivity introduced by vegetation, surface wetness, water bodies and terrain. Conner and Petty (1998) indicate that the spectral information contained in the SSM/I data over land can explain only about 30% of the variance present in the radar or the rain gauge observations over land. From the above discussion, we conclude that because of the spatial inhomogeneities and the uncertainties in the nature of the hydrometeors, radiative transfer models do not succeed in retrieving rain rate over land. Thus, in order to get good rain retrievals over land and ocean, more information in addition to the microwave radiometer spectral measurements is needed.

In the studies of Prabhakara et al. (1998, 1999), the rain area in a mesoscale geographic region (~ 2° lat x 3° lon) deduced from the SSM/I data is provided as additional information to estimate the mesoscale area-average rain rate. Those

---

[1] *Radiometer of the Defense Meteorological Satellite Program (DMSP) that has 19, 37, and 85 GHz channels in dual polarization and a 22 GHz channel in vertical polarization. This radiometer observes the Earth's surface and atmosphere in a conical scan with an incidence angle of ~ 50° (for more details see Hollinger et al., 1985).*

[2] *Tropical Rainfall Measuring Mission. On board the TRMM satellite, there is the cross-track-scanning Precipitation Radar (PR) and the conical-scanning TRMM Microwave Imager (TMI) (see Simpson et al., 1996).*

studies indicate that the rain area in a mesoscale region serves as a more important factor in estimating area-average rain rate than the spectral information given by the SSM/I data. This mesoscale area-average rain retrieval approach is widely used and has its basis in the Area Time Integral concepts of Doneaud et al. (1984) and Lopez et al. (1989). A useful inference from these studies is that the atmospheric dynamics that lead to the total volume of rain in a mesoscale region are coupled to the rain area in that region.

Utilizing a similar conceptual framework, in the present study we will attempt to use the spatial, and the spectral, information given by the TMI radiometer data to discriminate between convective and stratiform rain on a thunderstorm scale, and thereby improve rain retrieval capability. The TMI radiometer is similar to the SSM/I, except that it has two additional spectral channels (vertical and horizontal polarization) at 10 GHz. Furthermore, because of the lower altitude of the TRMM satellite, the spatial resolution of the TMI radiometer is about two times finer compared to SSM/I. This finer resolution, in conjunction with the spectral information, offers an opportunity to discriminate convective rain from stratiform rain.

We may remark that the vertical resolving capability of the radar gives it a distinct advantage over the passive microwave radiometer. Furthermore, radar back scatter measurements have a d^6 dependence on the rain drop diameter (Battan, 1973), while radiometer observations tend to have about a d^3 dependence (e.g., Olson, 1996). Both of these properties of the radar help it to isolate the rain layer and to get a more robust estimate of rain rate. However, it may be remarked that rain rate estimates based on radar data are linked to the rain drop size distribution (DSD).

There is a difference in DSD between convective and stratiform rain. Tokay and Short (1996)

show with disdrometer data that the mode radius of the DSD for a given rain rate in stratiform rain is larger. This difference, if it is not accounted for, could lead to an overestimation of stratiform rain rate by about a factor of two. However, difference in DSD associated with convective and stratiform rain can be inferred with the help of horizontal inhomogeneity in rain rate (Steiner et al., 1995). From such inference, errors in rain rate estimation can be minimized. In addition to this problem, there could be other temporal variabilities in DSD. Probable error in rain rate due to such DSD variability is estimated to be within ~ 50%. This error estimate is based on simulations of radar back-scatter using disdrometer observed DSD (R. Meneghini, personal communication). Because of these non-negligible errors, radar rain rates are calibrated with respect to surface rain gauges. An example of such calibration is that performed over Japan with the Automatic Meteorological Data Acquisition System (e.g., Oki et al., 1997).

Unlike radar observations, spectral information from measurements made by microwave radiometers have poor vertical resolution and ability to discriminate stratiform versus convective rain. Therefore, as shown in the study of Heymsfield et al. (1996), there are much larger errors associated with rain rates retrieved using radiometer spectral data. For these reasons, until better ground truth is available, we will use the TRMM Precipitation Radar (PR) rain estimates as a basis to develop our TMI rain retrieval method. When better ground truth is available, this TMI algorithm can be readily tuned with the help of such information.

In the TRMM mission, the TMI measurements cover a swath width of 760 km. On the other hand, PR measurements cover only the 220 km central portion of the TMI swath (Simpson et al., 1996). This much larger scanning capability of the TMI could be exploited to give more temporal and spatial coverage of rain information over land and ocean regions.

TMI Rain Rate Estimation

2. MODEL TO RETRIEVE RAIN RATE MAPS WITH CONVECTIVE AND STRATIFORM DISCRIMINATION BASED ON TMI DATA

Studies of Houze and Betts (1981) and Houze (1993, 1997) show that in Mesoscale Convective Systems (MCSs) there are thunderstorms or cumulonimbus clouds (Cbs) in different stages of growth. A Cb may contain a single cloud cell or multiple cloud cells. The scale of these Cbs may vary somewhat, but on average it is about 20 km. In a gross fashion, a given Cb may be categorized as young, mature, or decaying according to its age. The young Cbs have cloud cells with moderate to strong vertical motions of several ms^{-1}, in which rain drops grow primarily through the coalescence mechanism. Because these young Cbs have not grown deep into the atmosphere, there are relatively small amounts of ice particles in these Cbs. The mature Cbs have strong vertical motions which reach high altitudes and produce larger amounts of frozen rain drops and graupel. Moderate and intense rain rates reflect the strength of the narrow updrafts in the young and mature Cbs, respectively. For both the young and mature Cbs, the strength of the vertical motions and the rain rate decrease rapidly toward the Cb edge. On the contrary, in the decaying Cbs the vertical motions are relatively weak (~ 1–3 ms^{-1}), which allows sufficient time for the growth of falling ice crystals by

Table 1. Updraft characteristics, hydrometeor growth mechanisms, and hydrometeor characteristics associated with young, mature, and decaying Cbs.

Cb Type	Updraft Characteristics	Hydrometeor Growth Mechanism	Hydrometeor Characteristics
Young	Strong (> 3 ms^{-1}) Narrow (~ 1–3 km)	Collision and coalescence	Small amounts of dense frozen rain drops and graupel
	Limited in height to a few km above freezing level		Convective rain
Mature	Strong (> 3 ms^{-1}) Narrow (~ 1–3 km)	Collision and coalescence	Large amounts of dense frozen rain drops and graupel
	Extend to heights well above freezing level		Convective rain
Decaying	Weak (~ 1–3 ms^{-1}) Broad (> 5 km)	Vapor deposition and aggregation of ice particles	Large amounts of ice aggregates (snow)
	Generally above the freezing level		Stratiform rain

deposition of water vapor. In turn, these ice crystals form ice aggregates before entering the melting layer, and then melt to form rain below this layer. This type of rain is stratiform in nature and relatively weak, but is more homogeneous in a given area. In this study, we will take advantage of this simple cloud dynamics and microphysics background, as summarized in table 1, to help us develop a microwave radiometer rain retrieval scheme that can take into account the nature of convective and stratiform rain.

In figure 1a, a map of a rain event over the Southeast United States on 5 June 1998 is depicted using the TMI T85 horizontal polarization data. The horizontal polarization is preferred because of the surface emissivity effect, which gives it a larger dynamic range over land and ocean compared to the vertical polarization data. We emphasize the 85 GHz TMI data in this study because, of all the channels of this radiometer, the 85 GHz channel has the finest spatial resolution and the highest extinction to ice and liquid hydrometeors. In particular, the scattering of microwave radiation, which according to radiative transfer theory results in a depression in the 85 GHz data, is strongly related to cloud ice content (Wu and Weinman, 1984). The rain rate map deduced from the PR data for the same time period (within 2 min) is shown in figure 1b. These maps represent the 220 km central portion of the TMI swath.

The PR rain-rate map shown in figure 1b has a character similar to rain maps derived from conventional radars (see for example Houze, 1993). In particular, the striking contrast between heavy rain rate in convective cells and weak rain rate present in the extensive stratiform region is faithfully reproduced in the PR data. The commonly observed log-normal type of frequency distribution of rain rate (Jones and Sims, 1978) is also revealed by the PR rain rates. This frequency distribution is illustrated in figure 1c using the PR rain rates displayed in figure 1b. These properties of the PR data reinforce their credibility.

From the map of PR rain rate shown in figure 1b, we discern that there is a squall line composed of several intense Cbs. Furthermore, there are several other weaker Cbs. Some of these weaker Cbs are present in the extensive stratiform region. By comparing the PR rain-rate map with the map of T85, we notice there are local minima in T85 ($T85_{min}$), which correspond to the location of rain maxima in the PR rain map. These rain maxima represent the thunderstorms or Cbs. We may point out that a local minimum in T85 can be defined in the TMI data with respect to the brightness temperature values of its four neighboring footprints given by the TMI conical scans, as shown in figure 2. Apparently, $T85_{min}$ can be produced by dense ice particles that can strongly scatter microwave radiation in the narrow convective cells; or they can be produced by frozen and melting ice aggregates that can weakly scatter microwave radiation over a broader area. We note from figure 1a that we cannot identify the three different types of Cbs based simply on the magnitude of $T85_{min}$. In order to do such identification, we need to infer the spatial structure of the hydrometeors in the Cb. This structure can be assessed from the mean of the absolute values of the spatial gradients, i.e., $\overline{|dT85/dr|}$, within each Cb. Here, r represents the distance between a point in the Cb and the location of $T85_{min}$. This $\overline{|dT85/dr|}$ is determined utilizing the four neighboring footprint values as illustrated in figure 2, and it is analagous to the Laplacian ($\nabla^2 T85$) with an additional condition that the T85 at the center point is a minimum.

Given the information $T85_{min}$ and $\overline{|dT85/dr|}$, we have developed, using PR rain rate as a guide, the following simple conceptual model to identify young, mature, and decaying Cbs. First, because of narrow and relatively strong updrafts in the cloud cells of young and mature Cbs that contain dense ice hydrometeors, the mean gradient around $T85_{min}$, $\overline{|dT85/dr|}$, is large compared to that in the decaying Cbs. This gives us a criterion to separate decaying Cbs from convectively active young and mature Cbs. Second, as a result of larger amounts of frozen rain drops and grau
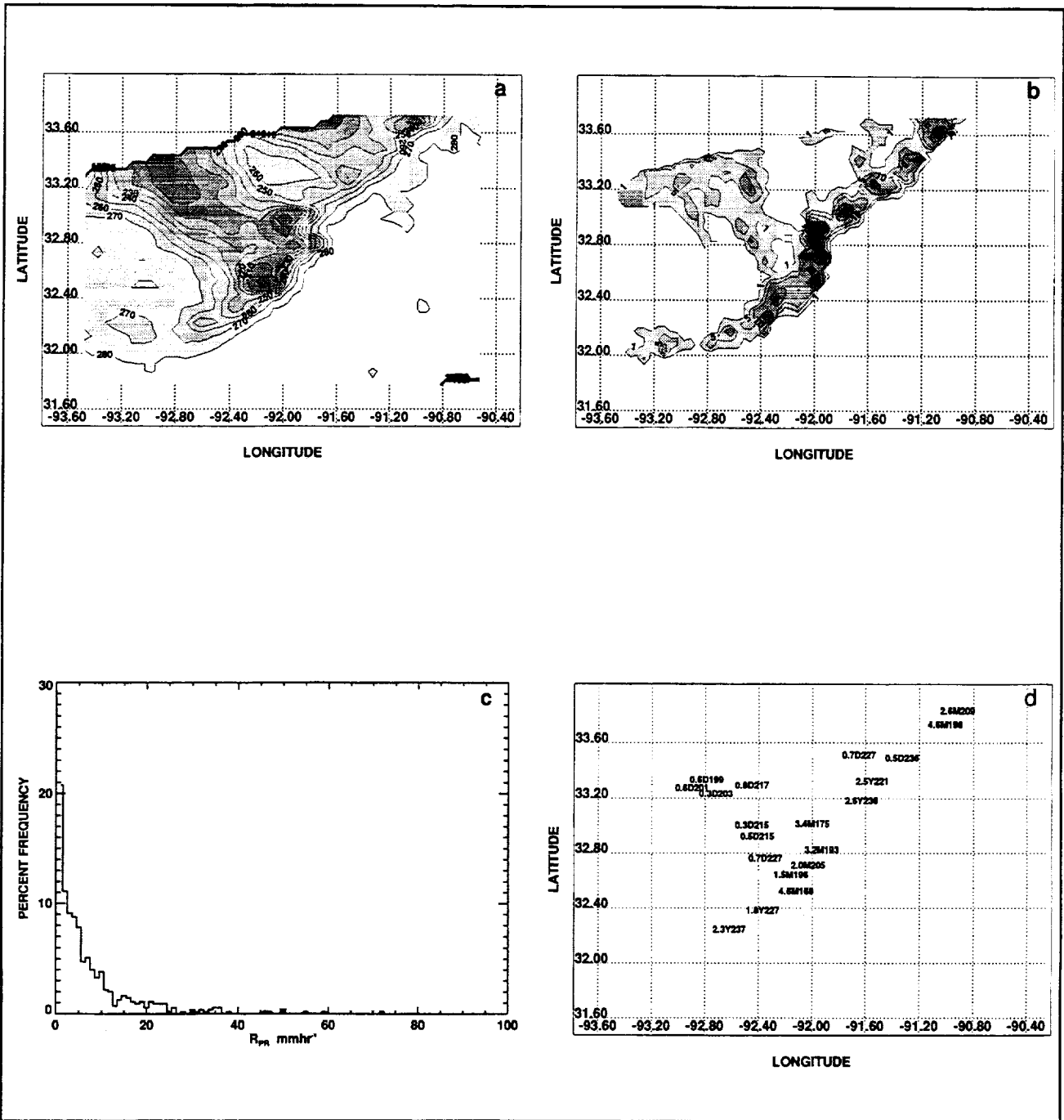
Figure 1. Data pertaining to a Mesoscale Convection System over the Southeast U.S. on 5 June 1998.
a) Map of 85 GHz brightness temperature, T85 (K), deduced from TMI.
b) Map of TRMM Precipitation Radar rain rate R_{PR} (mmhr^{-1}).
c) Frequency distribution of rain rate for this event deduced from PR data.
d) Map of minima of T85 for this rain event indicating location of different types of thunderstorms—young (Y), mature (M) and decaying (D). The numbers shown on the left and right of the symbols Y, M, and D indicate the magnitude of $|\overline{d\,T85/dr}|$ and $T85_{min}$.

When $T_0 < T_1, T_2, T_3$ and T_4

Then $T_{min} = T_0$

$$\overline{\frac{dT}{dr}} = \frac{A(T_1 + T_2) + B(T_3 + T_4) - 4T_0}{4}$$
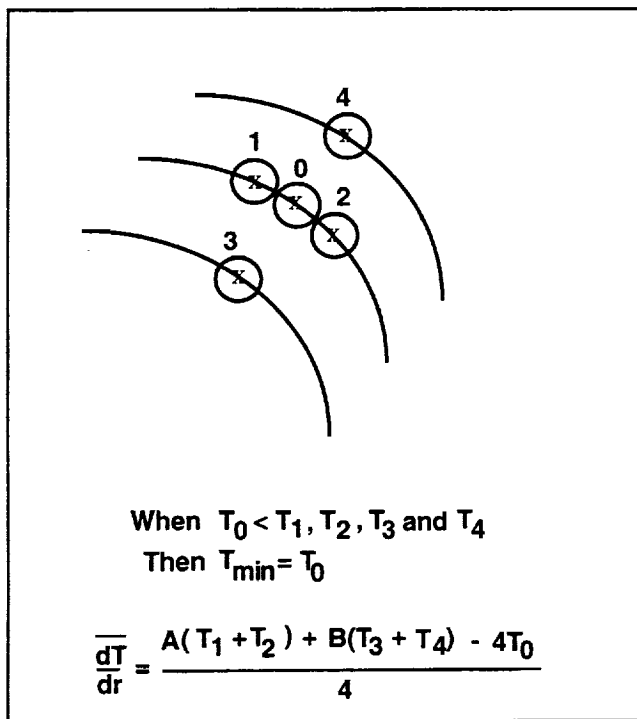
Figure 2. Illustration of the method to determine the location of T85 minimum (T85$_{min}$) and the mean spatial gradient $|\overline{d\,T85/dr}|$ around this minimum. The solid curves represent the conical scan of the TMI radiometer, and the circles represent the footprints. Along the scan, the separation between footprints is about 4.6 km, while the separation between scans is about 13.9 km. In the illustration, the coefficients A and B correspond to appropriate weighting factors.

pel, we expect mature Cbs to have magnitudes of T85$_{min}$ that are small in comparison to those found in young Cbs. Thus, by comparing the T85 minima, the young and mature Cbs can be separated. In order to illustrate the correspondence between the Cbs indicated by the PR and the T85 data respectively shown in figures 1a and 1b, a map of the locations of T85$_{min}$ for the rain event of 5 June 1998 is shown in figure 1d. The magnitudes of T85$_{min}$ and $|dT85/dr|$ for each Cb are also shown in this figure. The criteria chosen in our model to discriminate the young, mature, and decaying Cbs are presented in table 2. These criteria, although subjective, are commensurate with models of radiative transfer that consider dense and less dense ice particles. The magnitudes of T85$_{min}$ and $|\overline{dT85/dr}|$ given in table 2 were determined by examining the spatial patterns of T85 and the rain rates given by the PR for several rain events on land and ocean areas within 35° N and 35° S.

In the present rain retrieval model, in order to blend the stratiform and convective rain rates in a smooth fashion, a weak background rain rate R_s is assigned to all the areas where T85 is less than 260K. This background rain rate accounts for the stratiform rain in the areas where Cbs are absent. A linear relationship between rain rate

Table 2. Criteria to discriminate young, mature, and decaying Cbs.

Cb Type	85 GHz Minimum	85 GHz Mean Gradient
Young	255 K > T85$_{min}$ > 210 K	$|\overline{d\,T85/dr}| > 1$ Kkm^{-1}
Mature	T85$_{min}$ < 210 K	$|\overline{d\,T85/dr}| > 1$ Kkm^{-1}
Decaying	255 K > T85$_{min}$	0 Kkm^{-1} < $|\overline{d\,T85/dr}|$ < 1 Kkm^{-1}

6

TMI Rain Rate Estimation

and T85 is used to estimate this background rain rate. This relationship is given by the equation

$$R_S = (260 - T85)\{dR_{PR}/dT85\}, \qquad (1)$$

where R_{PR} stands for rain rate observed by the Precipitation Radar. Based on observations, the sensitivity factor $dR_{PR}/dT85$ is set equal to 0.12.

In our model, the rain rate in each Cb is superimposed on the background rain rate R_S. Each Cb is assumed to have a circular area with a radius of 10 km, with its center coinciding with the location of the pixel that has the minimum value $T85_{min}$. We determine the Cb type as described earlier (see table 2). Then based on the type, we estimate the mean rain rate in a Cb using one of the following three linear relationships:

Young Cbs:

$$\overline{R}_Y = F_{10}[(255 - T85_{min})\{d\overline{R}_{pr}/dT85_{min}\}_Y] \quad (2a)$$

Mature Cbs:

$$\overline{R}_M = F_{10}[(255 - 210)\{d\overline{R}_{pr}/dT85_{min}\}_Y +$$
$$(210 - T85_{min})\{d\overline{R}_{pr}/dT85_{min}\}_M] \,(2b)$$

Decaying Cbs:

$$\overline{R}_D = F_{10}[(255 - T85_{min})\{d\overline{R}_{pr}/dT85_{min}\}_D]. \quad (2c)$$

where $\overline{R}_Y$, $\overline{R}_M$, and $\overline{R}_D$ stand for mean rain rates of young, mature and decaying Cbs, respectively. This rain rate is superimposed on R_S to get total rain rate in each Cb. In equations 2a and 2b, corresponding to the convectively active young and mature Cbs, the sensitivity factors $(d\overline{R}_{PR}/dT85_{min})_Y$ and $(d\overline{R}_{PR}/dT85_{min})_M$ are used, where $\overline{R}_{PR}$ represents the radar derived mean rain rate over the area of a Cb. As shown in equation 2c, another sensitivity factor $(d\overline{R}_{PR}/dT85_{min})_D$ is used for the decaying Cbs. These sensitivity factors are optimized with the help of the TMI and PR observations of a small sample of MCS cases. Over the ocean, the term F_{10} is set to vary linearly between 0.0 and 1.0 as the 10 GHz

brightness temperature varies between 100 and 200 K, respectively. This can be expressed as

$$F_{10} = \begin{cases} 0.0 & T10 < 100K \\ (T10-100)/100 & 100K \le T10 \le 200K \\ 1.0 & T10 > 200K \end{cases} \quad (2d)$$

From equation 2d, F_{10} is assigned a value of 1.0 over land regions, since T10 is greater than 200 K. Rain rate where T85 is at and above 260 K is assumed to be zero. We may note that in the present study the polarization in the 85 GHz, i.e., P85, is used to discriminate open ocean and wet surfaces on land from precipitating clouds where T85 is less than 260 K. A value of P85 greater than 15 K is used to screen out these surfaces. In table 3, we are presenting the magnitude of $(d\overline{R}_{PR}/dT85_{min})$ for all Cb types.

As already indicated, the present rain retrieval model based on TMI data can estimate the mean rain rate in the Cbs on a scale of 20 km. In order to obtain the pattern of rain rate R everywhere in an MCS, including inside the Cbs, we use a simple interpolation procedure. As an example, we show below the interpolation equation applicable to young Cbs:

$$R = R_S + [R_Y - \{R_Y/(T85_{Max} - \overline{T85})\}(T85 - \overline{T85})]. \quad (3)$$

Similar equations are applied to the mature and decaying Cbs. Here, T85 stands for the 85 GHz brightness temperature at any given point in a Cb, and $T85_{Max}$ and $\overline{T85}$ stand for the maximum and mean values of T85 in that Cb. Utilizing equations 1, 2 and 3, in the present method we have derived the rain rate R everywhere in an MCS where T85 is less than 260 K.

The relationship between $T85_{min}$ and $\overline{R}_{PR}$ is not necessarily linear. For simplicity, in equations 2a, 2b, and 2c, we have adopted a linear approximation. Because of this reason, the $d\overline{R}_{PR}/dT85_{min}$ values shown in table 3 have been optimized with a tuning procedure. This tuning procedure is discussed in the following section.

Table 3. Sensitivity of $T85_{min}$ to the Cb mean rain rate $\overline{R}_{PR}$ applicable to tropical land and ocean regions.

Cb Type	85 GHz Minimum	Sensitivity Factors $d\overline{R}_{PR}/dT85_{min}$
Young	$255\ K > T85_{min} > 210\ K$	$0.25\ mmhr^{-1}K^{-1}$
Mature	$T85_{min} < 210\ K$	$0.35\ mmhr^{-1}K^{-1}$
Decaying	$255\ K > T85_{min}$	$0.12\ mmhr^{-1}K^{-1}$

3. TUNING PROCEDURE FOR THE RAIN RETRIEVAL MODEL

For the purpose of optimization or tuning, we use a dependent sample of six rain events on land, and another sample of six rain events on ocean. For land, details pertaining to these events are listed in tables 4a and 4b. For ocean, these details are listed in tables 5a and 5b.

In the initial stage of the tuning procedure, preliminary estimates of the sensitivity factors needed in the retrieval algorithm are deduced as follows. For a given rain event, we identify the positions and the categories of Cbs with the help of $T85_{min}$ and $|dT85/dr|$. Then, for each Cb in that event, we compute $\overline{R}_{PR}$ from the PR data. A similar procedure is applied to the remaining rain events, and a data set consisting of Cbs and their corresponding values of $\overline{R}_{PR}$ is developed. From this data set, we isolate one subset consisting of young Cbs. For that one subset, we determine a best linear fit between $T85_{min}$ and $\overline{R}_{PR}$. The slope of this linear fit for that Cb category gives us a preliminary estimate of the sensitivity factor $\{d\overline{R}_{PR}/dT85_{min}\}_Y$. In an analagous fashion, from the mature and decaying data subsets we determine preliminary values of the sensitivity factors $\{d\overline{R}_{PR}/dT85_{min}\}_M$ and $\{d\overline{R}_{PR}/dT85_{min}\}_D$ applicable to mature and decaying Cbs, respectively.

As stated earlier, the relationship between $T85_{min}$ and rain rate is not necessarily a linear function. For this reason, the first guess or preliminary estimates of the sensitivity factors are iteratively refined until a desired accuracy of the algorithm is reached. In this iterative procedure, these estimates of the sensitivity factors are used along with equations 1, 2, and 3, to retrieve rain rates R over an area of about $2°x 3°$ (lat x lon) for all rain events. Note that the $2°x 3°$ area is representative of the mesoscale region covered by the 220 km scan width of the PR. Utilizing the values of R in the $2°x 3°$ region that overlap with the PR scan area, the following seven quantities are calculated for each rain event:

• f^I, f^{II}, and f^{III}—quantities directly related to frequency of rain rate in three intervals, I) 1–10 mmhr^{-1}, II) 10–20 mmhr^{-1}, and III) greater than or equal to 20 mmhr^{-1}. These three quantities are simply the fractional rain areas corresponding to these three rain intervals:

• $\langle R \rangle_I$, $\langle R \rangle_{II}$, and $\langle R \rangle_{III}$—mean rate rates in the three intervals;

• $\langle R \rangle_A$—area-average rain rate in the overlap area of the $2°x 3°$ region.

To improve the first guess of the sentivity factors, the means of each of the seven quantities $\overline{\langle R \rangle}_I$, $\overline{\langle R \rangle}_{II}$, $\overline{\langle R \rangle}_{III}$, f^I, f^{II}, and f^{III}, and $\langle R \rangle_A$ are computed from the dependent sample of six rain events separately for the land and ocean MCS

Table 4a. Land—dependent and independent MCS events and the associated fractional rain area statistics. The fractional rain area is calculated for each of the following rain rate intervals: I) 1–10 mmhr^{-1}, II) 10–20 mmhr^{-1}, and III) greater than or equal to 20 mmhr^{-1}.

Dependent Cases

Day/Yr	Lat	Lon	f^I	f^I_{PR}	f^I_{TMI}	f^{II}	f^{II}_{PR}	f^{II}_{TMI}	f^{III}	f^{III}_{PR}	f^{III}_{TMI}
156/98	32.8	-92.0	0.21	0.19	0.09	0.03	0.04	0.12	0.02	0.02	0.00
169/98	26.9	115.7	0.57	0.51	0.35	0.04	0.03	0.25	0.02	0.01	0.00
180/98	32.8	160.0	0.27	0.28	0.11	0.04	0.06	0.21	0.02	0.04	0.00
201/98	28.9	116.0	0.29	0.25	0.07	0.02	0.02	0.18	0.03	0.01	0.00
271/98	31.5	-87.0	0.76	0.72	0.48	0.06	0.10	0.35	0.02	0.03	0.00
362/98	-26.7	-58.0	0.70	0.52	0.06	0.18	0.16	0.86	0.08	0.12	0.03
MEAN			**0.47**	**0.41**	**0.19**	**0.06**	**0.07**	**0.33**	**0.03**	**0.04**	**0.01**

Independent Cases

Day/Yr	Lat	Lon	f^I	f^I_{PR}	f^I_{TMI}	f^{II}	f^{II}_{PR}	f^{II}_{TMI}	f^{III}	f^{III}_{PR}	f^{III}_{TMI}
146/98	35.0	-89.5	0.48	0.38	0.17	0.06	0.11	0.37	0.04	0.08	0.0
156/98	35.0	-89.1	0.62	0.47	0.12	0.10	0.13	0.56	0.06	0.09	0.02
159/98	12.5	-1.4	0.34	0.17	0.03	0.04	0.02	0.24	0.03	0.02	0.0
160/98	4.4	-66.2	0.45	0.47	0.39	0.02	0.02	0.05	0.0	0.0	0.0
162/98	33.0	-99.5	0.29	0.19	0.15	0.08	0.02	0.19	0.06	0.09	0.06
162/98	31.7	115.6	0.36	0.31	0.25	0.02	0.01	0.04	0.0	0.0	0.0
171/98	25.8	115.0	0.22	0.19	0.17	0.01	0.02	0.02	0.02	0.01	0.0
186/98	24.0	81.5	0.44	0.49	0.18	0.06	0.06	0.31	0.03	0.03	0.0
19/99	-17.9	29.8	0.32	0.40	0.19	0.04	0.03	0.12	0.03	0.02	0.0
44/99	-17.2	127.5	0.43	0.28	0.15	0.05	0.05	0.31	0.06	0.04	0.01
MEAN			**0.40**	**0.34**	**0.18**	**0.05**	**0.05**	**0.22**	**0.03**	**0.04**	**0.01**

Table 4b. Land—dependent and independent MCS events and the associated mesoscale-mean rain statistics. The mean rain rate is calculated for each of the following rain rate intervals: I) 1–10 mmhr^{-1}, II) 10–20 mmhr^{-1}, and III) greater than or equal to 20 mmhr^{-1}.

Dependent Cases

Day/Yr	Lat	Lon	$\langle R \rangle_{III}$	$\langle R_{PR} \rangle_{III}$	$\langle R_{TMI} \rangle_{III}$	$\langle R \rangle_{A}$	$\langle R_{PR} \rangle_{A}$	$\langle R_{TMI} \rangle_{A}$
156/98	32.8	-92.0	31.3	32.0	0.0	1.7	1.9	2.0
169/98	26.9	115.7	33.4	30.0	0.0	2.9	2.3	5.1
180/98	32.8	160.0	30.3	30.5	0.0	2.1	3.1	3.0
201/98	28.9	116.0	32.8	25.1	0.0	2.1	1.1	2.6
271/98	31.5	-87.0	29.3	27.0	0.0	3.6	5.1	7.1
362/98	-26.7	-58.0	42.1	45.2	20.9	10.1	9.9	12.1
MEAN			**33.2**	**31.6**	**3.2**	**3.8**	**3.9**	**5.3**

Independent Cases

Day/Yr	Lat	Lon	$\langle R \rangle_{III}$	$\langle R_{PR} \rangle_{III}$	$\langle R_{TMI} \rangle_{III}$	$\langle R \rangle_{A}$	$\langle R_{PR} \rangle_{A}$	$\langle R_{TMI} \rangle_{A}$
146/98	35.0	-89.5	39.4	38.2	0.0	4.4	6.3	5.6
156/98	35.0	-89.1	40.2	44.2	25.5	6.8	7.7	8.4
159/98	12.5	-1.4	37.3	30.5	20.0	3.2	1.4	3.2
160/98	4.4	-66.2	26.0	32.3	0.0	1.5	1.7	2.8
162/98	33.0	-99.5	61.6	75.1	20.8	5.7	7.8	4.8
162/98	31.7	115.6	24.8	21.5	0.0	1.2	.7	2.0
171/98	25.8	115.0	35.7	34.9	0.0	1.3	1.1	1.2
186/98	24.0	81.5	33.3	28.4	0.0	3.4	3.4	4.8
19/99	-17.9	29.8	36.8	28.8	20.0	2.4	2.0	2.6
44/99	-17.2	127.5	42.3	32.8	20.5	5.0	3.0	5.2
MEAN			**37.7**	**36.7**	**10.7**	**3.5**	**3.5**	**4.1**

TMI Rain Rate Estimation

Table 5a. Ocean—dependent and independent MCS events and the associated fractional rain area statistics. The fractional rain area is calculated for each of the following rain rate intervals: I) 1–10 mmhr^{-1}, II) 10–20 mmhr^{-1}, and III) greater than or equal to 20 mmhr^{-1}.

Dependent Cases

Day/Yr	Lat	Lon	f^I	f^I_{PR}	f^I_{TMI}	f^{II}	f^{II}_{PR}	f^{II}_{TMI}	f^{III}	f^{III}_{PR}	f^{III}_{TMI}
159/98	-9.5	85.0	0.33	0.44	0.46	0.02	0.02	0.17	0.01	0.00	0.01
162/98	13.6	-105.2	0.41	0.39	0.51	0.02	0.02	0.06	0.01	0.01	0.03
314/98	5.5	147.2	0.63	0.61	0.62	0.06	0.08	0.35	0.04	0.03	0.06
7/99	4.5	156.0	0.45	0.46	0.55	0.04	0.03	0.14	0.01	0.01	0.03
24/99	6.0	148.5	0.64	0.65	0.43	0.08	0.06	0.38	0.05	0.05	0.08
70/99	-25.2	54.0	0.59	0.58	0.54	0.02	0.02	0.20	0.00	0.00	0.01
MEAN			**0.51**	**0.52**	**0.52**	**0.04**	**0.04**	**0.22**	**0.02**	**0.02**	**0.04**

Independent Cases

Day/Yr	Lat	Lon	f^I	f^I_{PR}	f^I_{TMI}	f^{II}	f^{II}_{PR}	f^{II}_{TMI}	f^{III}	f^{III}_{PR}	f^{III}_{TMI}
154/98	6.3	-13.0	0.59	0.47	0.64	0.02	0.04	0.25	0.01	0.02	0.01
158/98	21.0	118.2	0.38	0.28	0.48	0.01	0.01	0.04	0.01	0.02	0.02
184/98	3.9	-91.8	0.47	0.45	0.56	0.04	0.06	0.15	0.03	0.03	0.05
244/98	26.1	-90.6	0.45	0.40	0.59	0.04	0.06	0.14	0.02	0.02	0.04
269/98	8.5	-129.8	0.41	0.36	0.46	0.03	0.03	0.13	0.0	0.0	0.01
335/98	1.0	147.0	0.31	0.24	0.34	0.01	0.01	0.03	0.01	0.01	0.01
63/99	-0.4	-36.0	0.55	0.36	0.45	0.05	0.06	0.14	0.02	0.02	0.03
65/99	-14.4	102.4	0.71	0.64	0.62	0.06	0.05	0.12	0.04	0.06	0.12
68/99	-27.0	-29.6	0.38	0.27	0.47	0.06	0.05	0.13	0.03	0.04	0.06
73/99	-25.9	168.8	0.59	0.47	0.54	0.01	0.01	0.06	0.01	0.01	0.02
MEAN			**0.48**	**0.39**	**0.52**	**0.03**	**0.04**	**0.12**	**0.02**	**0.02**	**0.04**

Table 5b. Ocean—dependent and independent MCS events and the associated mesoscale-mean rain statistics. The mean rain rate is calculated for each of the following rain rate intervals: I) 1–10 mmhr^1, II) 10–20 mmhr^1, and III) greater than or equal to 20 mmhr^1.

Dependent Cases

Day/Yr	Lat	Lon	$\langle R \rangle_{III}$	$\langle R_{PR} \rangle_{III}$	$\langle R_{TMI} \rangle_{III}$	$\langle R \rangle_{A}$	$\langle R_{PR} \rangle_{A}$	$\langle R_{TMI} \rangle_{A}$
159/98	-9.5	85.0	21.8	20.0	24.5	1.5	1.6	4.2
162/98	13.6	-105.2	30.2	28.5	26.9	1.9	1.5	3.3
314/98	5.5	147.2	30.5	28.6	25.1	4.2	4.4	8.3
7/99	4.5	156.0	28.2	32.4	22.7	2.3	2.4	4.5
24/99	6.0	148.5	33.0	33.0	25.4	5.3	5.1	9.6
70/99	-25.2	54.0	20.3	21.2	24.6	2.3	1.9	4.9
MEAN			**27.3**	**27.3**	**24.9**	**2.9**	**2.8**	**5.7**

Independent Cases

Day/Yr	Lat	Lon	$\langle R \rangle_{III}$	$\langle R_{PR} \rangle_{III}$	$\langle R_{TMI} \rangle_{III}$	$\langle R \rangle_{A}$	$\langle R_{PR} \rangle_{A}$	$\langle R_{TMI} \rangle_{A}$
154/98	6.3	-13.0	29.3	29.4	25.3	2.0	2.5	5.7
158/98	21.0	118.2	32.5	37.9	25.8	1.5	1.6	2.2
184/98	3.9	-91.8	34.4	29.5	31.1	3.3	3.2	6.0
244/98	26.1	-90.6	30.8	30.4	27.3	2.6	2.8	5.1
269/98	8.5	-129.8	22.3	22.9	21.8	1.7	1.6	3.6
335/98	1.0	147.0	28.8	37.4	23.9	1.2	1.0	1.7
63/99	-0.4	-36.0	30.3	25.2	26.2	3.4	2.7	4.7
65/99	-14.4	102.4	40.6	44.2	40.1	4.9	4.9	8.7
68/99	-27.0	-29.6	29.4	35.0	24.9	3.2	3.0	5.0
73/99	-25.9	168.8	37.5	28.3	28.8	1.9	1.6	2.6
MEAN			**31.6**	**32.0**	**27.5**	**2.6**	**2.5**	**4.5**

cases. These means, denoted as $\langle \overline{R} \rangle_I$, $\langle \overline{R} \rangle_{II}$, $\langle \overline{R} \rangle_{III}$, $\overline{f}^I$, $\overline{f}^{II}$, $\overline{f}^{III}$, and $\langle \overline{R} \rangle_A$, are compared with those given by the PR. Based on this comparison, adjustments are made to the sensitivity factors until $\langle \overline{R} \rangle_I$, $\langle \overline{R} \rangle_{II}$, $\langle \overline{R} \rangle_{III}$, $\overline{f}^I$, $\overline{f}^{II}$, and $\overline{f}^{III}$, and $\langle \overline{R} \rangle_A$ given by the radiometer and the radar converge to within about 15%.

In order to estimate to within 15% the seven interdependent quantities $\langle \overline{R} \rangle_I$, $\langle \overline{R} \rangle_{II}$, $\langle \overline{R} \rangle_{III}$, $\overline{f}^I$, $\overline{f}^{II}$, $\overline{f}^{III}$, and $\langle \overline{R} \rangle_A$, we have used five parmameters: the three sensitivity factors given in equation 2, and the values of $T85_{min}$ and $|dT85/dr|$ that discriminate the young, mature, and decaying Cbs. We have adusted these parameters suitably to meet this desired goal.

In order to demonstrate the ability of the optimization procedure over land, in figures 3a, 3b, and 3c we are presenting maps of rain rate R_{PR}, R_{TMI}, and R for one dependent case—the rain event over Northern Argentina and Paraguay on 28 December 1998 found in table 4a. Here, the rain rates R_{PR} are R_{TMI} are the **Version 4** official products of the TRMM project derived respectively from Precipitation Radar and the microwave radiometer TMI. In this study, these rain rates are refered to as TRMM Standard Rain Rates. These maps can be compared to appreciate the merits of the present method. For further evaluation of the rain rate information given by these three maps, in figures 4a, 4b, and 4c we give the frequency distribution, i.e., f^I, f^{II}, f^{III}, of rain rate for R_{PR}, R_{TMI}, and R, respectively. By comparing the spatial and frequency distributions deduced from R_{PR} (figures 3a and 4a) with those of R_{TMI} (figures 3b and 4b), we find representation of stratiform and convective rain on land is not realistic in the TRMM Standard Rain Rate deduced from the microwave radiometer. On the other hand, similar information derived from R, as shown in figures 3c and 4c, compare better with that given by radar (figs. 3a and 4a).

To demonstrate the ability of the optimization procedure over ocean, in figures 5a, 5b, and 5c we are presenting maps of rain rate R_{PR}, R_{TMI},

and R for one dependent case—the 24 January 1999 rain event—that took place over the Equatorial Western Pacific (see table 5a). The frequency distributions f^I, f^{II}, and f^{III} of rain rate given by R_{PR}, R_{TMI}, and R are shown in Figures 6a, 6b, and 6c. By comparing the spatial and frequency distributions deduced from R_{PR} (figures 5a and 6a) with those of R_{TMI} (figures 5b and 6b), we find for this ocean case there is also poor agreement in the frequency distributions. Thus, stratiform and convective rain over ocean deduced by the TRMM Standard Rain Rate R_{TMI} does not compare well with that of the PR. The spatial and frequency distributions of rain rate derived using our algorithm, as shown in figures 5c and 6c, for this ocean case compare better with those given by radar (figures 5a and 6a). From these comparisons, we show for land and ocean regions that the rain rate R retrieved from our algorithm represents the information given by the PR significantly better than R_{TMI}.

The composite results, obtained from the six dependent MCS cases separately over land and ocean, shown in tables 4a, 4b, 5a, and 5b, reveal the ability of our method to reproduce the frequency distributions and the mesoscale-mean rain rates of the PR to within about 15%. This is achieved because of the ability of our method to discriminate convective rain from stratiform rain. However, since this sample of rain events is used in the tuning procedure, we have to demonstrate the applicability of this method with an independent set of rain events.
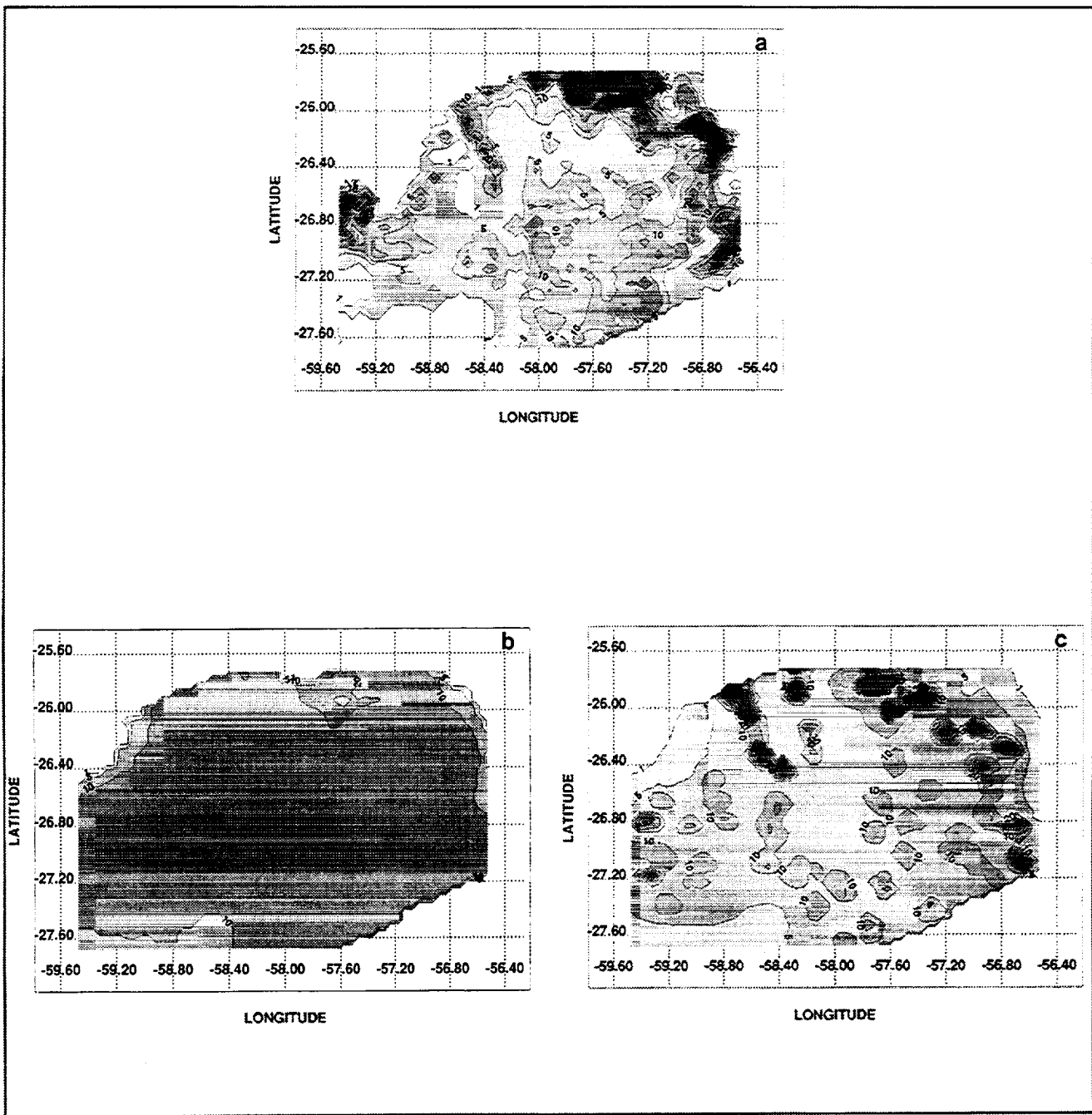
Figure 3. Maps of rain rate corresponding to a rain event that occurred over Northern Argentina and Paraguay on 28 December 1998.

a) PR rain rate, R_{PR} (mmhr^{-1}).

b) TRMM Standard Rain Rate. R_{TMI} (mmhr^{-1}), deduced from the microwave radiometer.

c) Rain rate, R (mmhr^{-1}), retrieved from our algorithm.

14
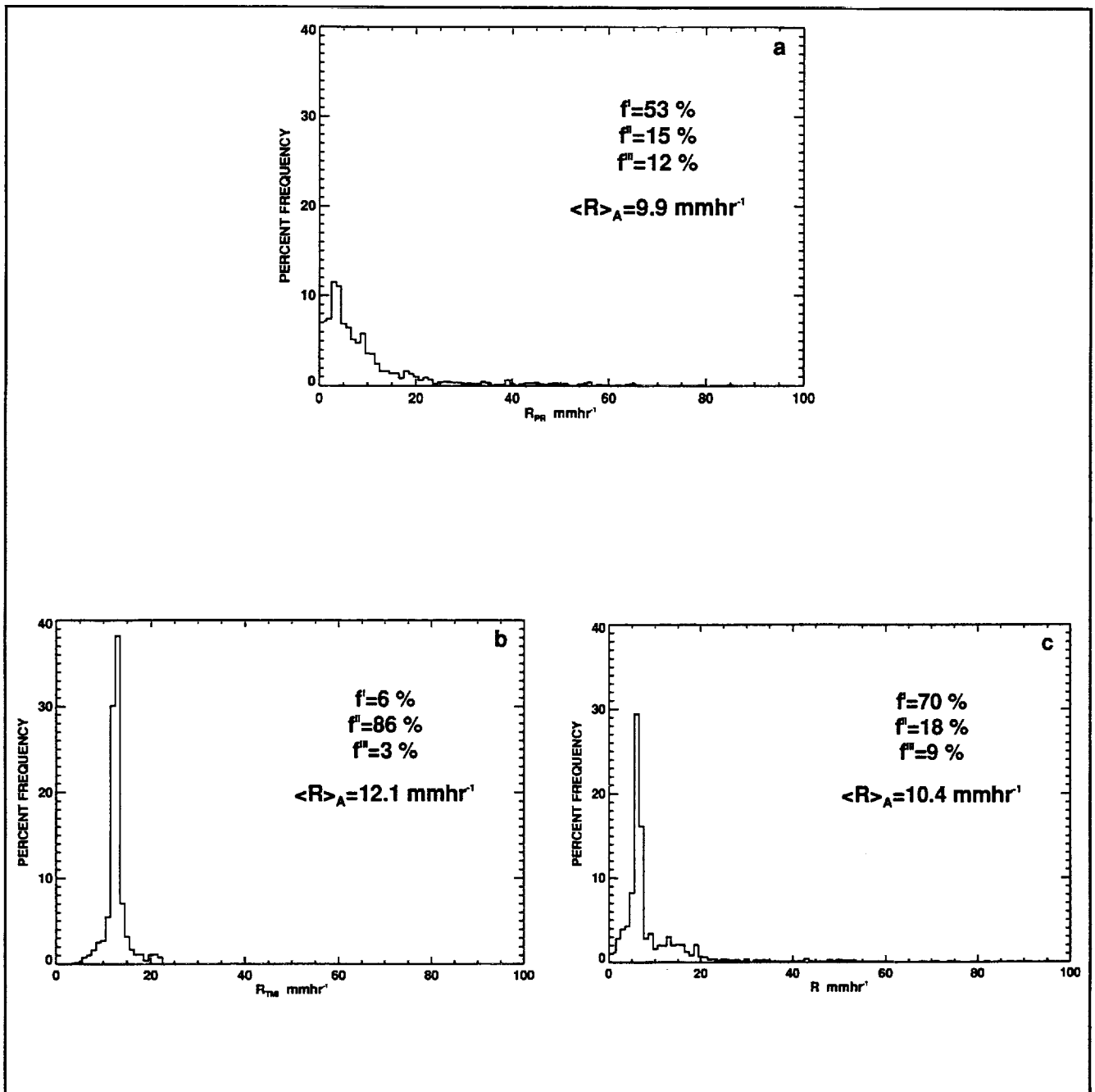
Figure 4. Frequency distributions of rain rate corresponding to the rain event depicted in figures 3a, 3b, and 3c.

a) PR rain rate, R_{PR} (mmhr^{-1}).

b) TRMM Standard Rain Rate, R_{TMI} (mmhr^{-1}), deduced from the microwave radiometer.

c) Rain rate, R (mmhr^{-1}), retrieved from our algorithm.
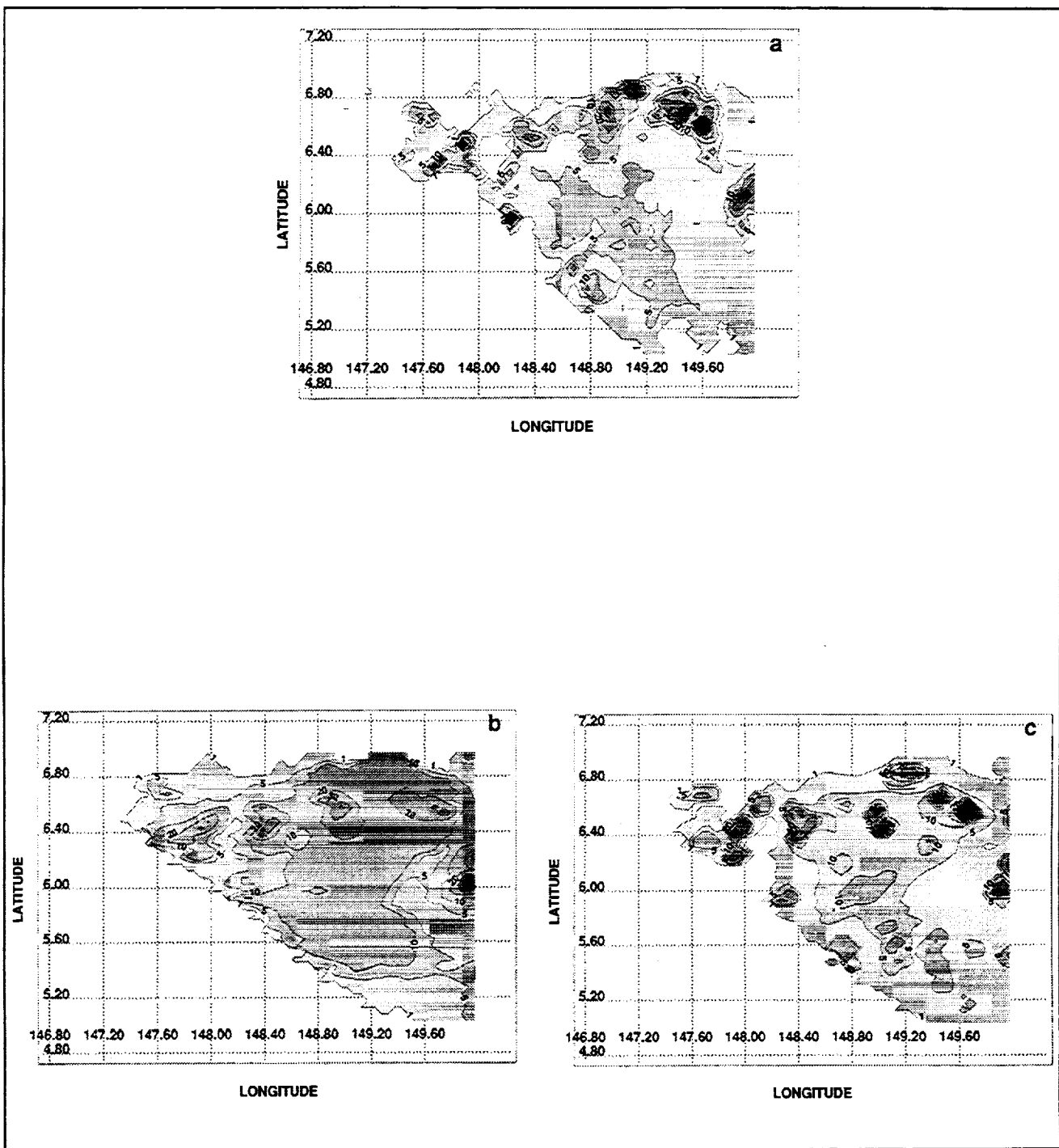
Figure 5. Maps of rain rate corresponding to a rain event that occurred over the Western Equatorial Pacific on 24 January 1999.

a) PR rain rate, R_{PR} (mmhr^{-1}).

b) TRMM Standard Rain Rate, R_{TMI} (mmhr^{-1}), deduced from the microwave radiometer.

c) Rain rate, R (mmhr^{-1}), retrieved from our algorithm.

TMI Rain Rate Estimation
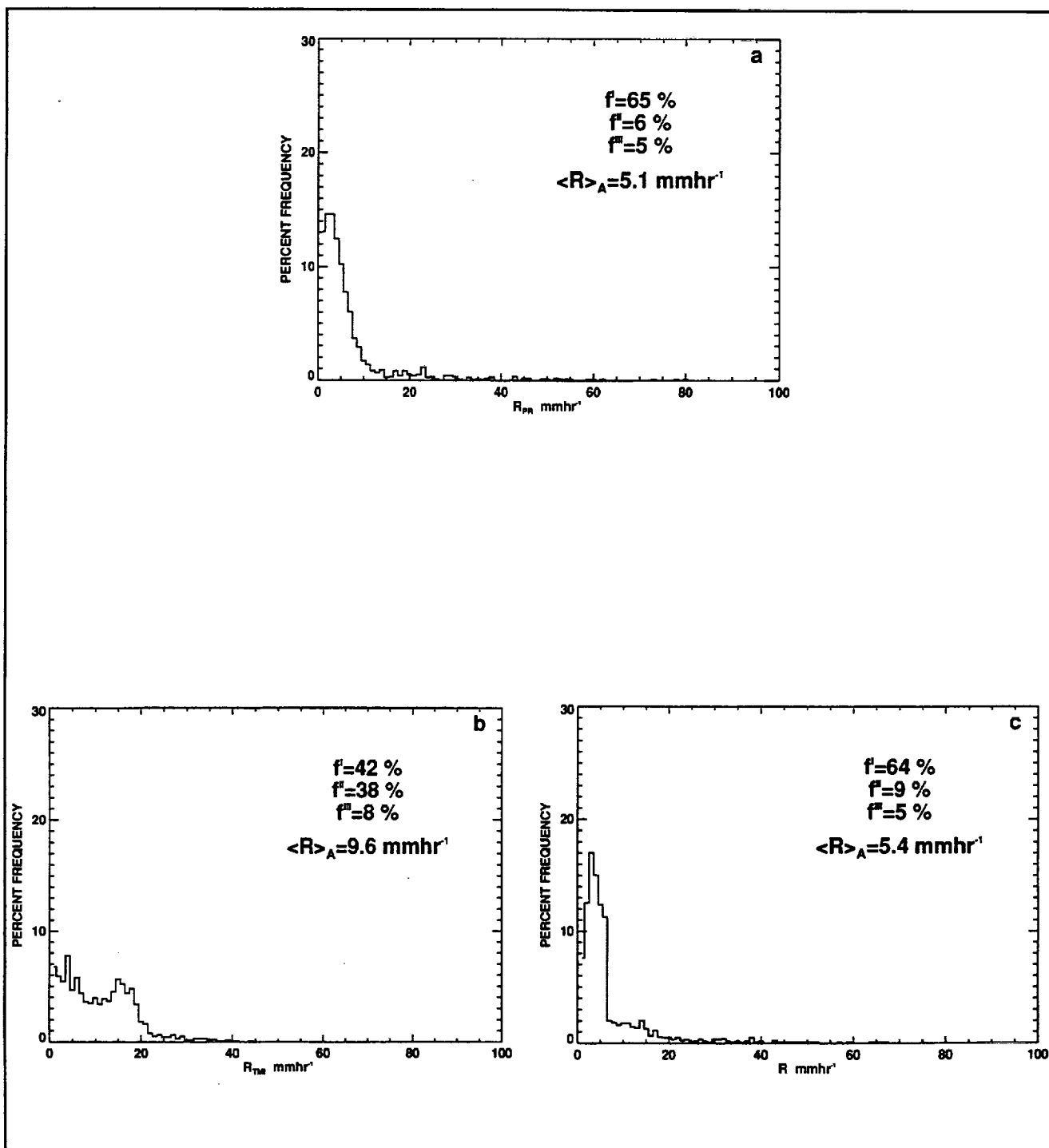
Figure 6. Frequency distributions of rain rate corresponding to the rain event depicted in figures 5a, 5b, and 5c.

a) PR rain rate, R_{PR} (mmhr^{-1}).

b) TRMM Standard Rain Rate, R_{TMI} (mmhr^{-1}), deduced from the microwave radiometer.

**c)** Rain rate, R (mmhr^{-1}), retrieved from our algorithm.

4. APPLICATION TO INDEPENDENT CASES

In order to show the general applicability of our algorithm, we have retrieved rain rates, R, for 10 independent cases over land, and the same number of cases over ocean. Also, the TRMM Standard Rain Rates R_{PR} and R_{TMI}, have been assembled for these cases. The relevant details pertaining to these events are listed in tables 4a and 4b for land, and in tables 5a and 5b for ocean.

In figure 7a, we compare the mesoscale area-average rain rates $\langle R \rangle_A$ and $\langle R_{PR} \rangle_A$ for the 10 rain events over land. In the same figure, we also compare the mesoscale area-average rain rates given by $\langle R_{TMI} \rangle_A$ with $\langle R_{PR} \rangle_A$. A similar scatterplot for the 10 rain events over ocean is given in figure 7b. From figures 7a and 7b, we find the area-average rain rates $\langle R \rangle_A$ and $\langle R_{TMI} \rangle_A$ correlate well with those given by PR. This comparison is not adequate to reveal the improvements in rain retrievals resulting from our algorithm.

The relative merits of our retrieval algorithm can be assessed by comparing the frequency distribution of rain rate. This comparison is done in a gross fashion in this study by considering frequency of rain rate in three intervals 1–10, 10–20 and greater than 20 mmhr[1] as discussed in the earlier section. The frequency of rain rate in these three intervals deduced from R agrees well with that given by the PR. On the contrary, the frequency distribution given by R_{TMI} shows a poor agreement. We present this information in tables 4a and 4b and tables 5a and 5b for the independent cases of land and ocean, respectively. Also in tables 4b and 5b, we present a comparison of $\langle \overline{R} \rangle_{III}$, $\langle \overline{R_{TMI}} \rangle_{III}$, and $\langle \overline{R_{PR}} \rangle_{III}$. However, such a comparison of mean rain rates in the intervals I and II is not done since these mean rain rates are strongly dependent on the rain rate limits of the intervals. This limitation does not apply to interval III.

In tables 4a, 4b, 5a, and 5b, we find, on the average for the 10 independent cases separately over land and ocean, that the frequency of rain rates in the three intervals 1–10, 10–20, and greater than 20 mmhr[1] differ by about 15% with respect to those of the PR. In addition, the corresponding $\langle \overline{R} \rangle_A$ and $\langle \overline{R} \rangle_{III}$ agree to within 5% of $\langle \overline{R_{PR}} \rangle_A$ and $\langle \overline{R_{PR}} \rangle_{III}$. Similar statistics based on R_{TMI} show a poor agreement with those of the PR. Based on these results, we contend that the algorithm developed here is capable of producing, for an independent sample of rain events, the area-average rain rate as well as the frequency distribution of rain over the area that is in fair agreement with that given by the radar.

The partitioning of convectively active thunderstorms, i.e., young and mature Cbs, from those that are decaying, is critical for the determination of latent heat input into the atmosphere. In figure 8, for all the MCS rain events over land and ocean, we show separately the frequency distributions of these active and decaying Cbs as a function of $T85_{min}$. From this figure, we see that the frequency distributions of the convectively active Cbs, both on land and ocean, tend to peak at a much colder $T85_{min}$ than the decaying Cbs. This vividly illustrates the stronger scattering effect of the dense ice particles in the active Cbs versus the less-dense ice aggregates in the decaying Cbs. This simple analysis presented in figure 8 lends support to the criterion $|dT85/dr|$ used to classify the convectively active and decaying Cbs (see table 2).
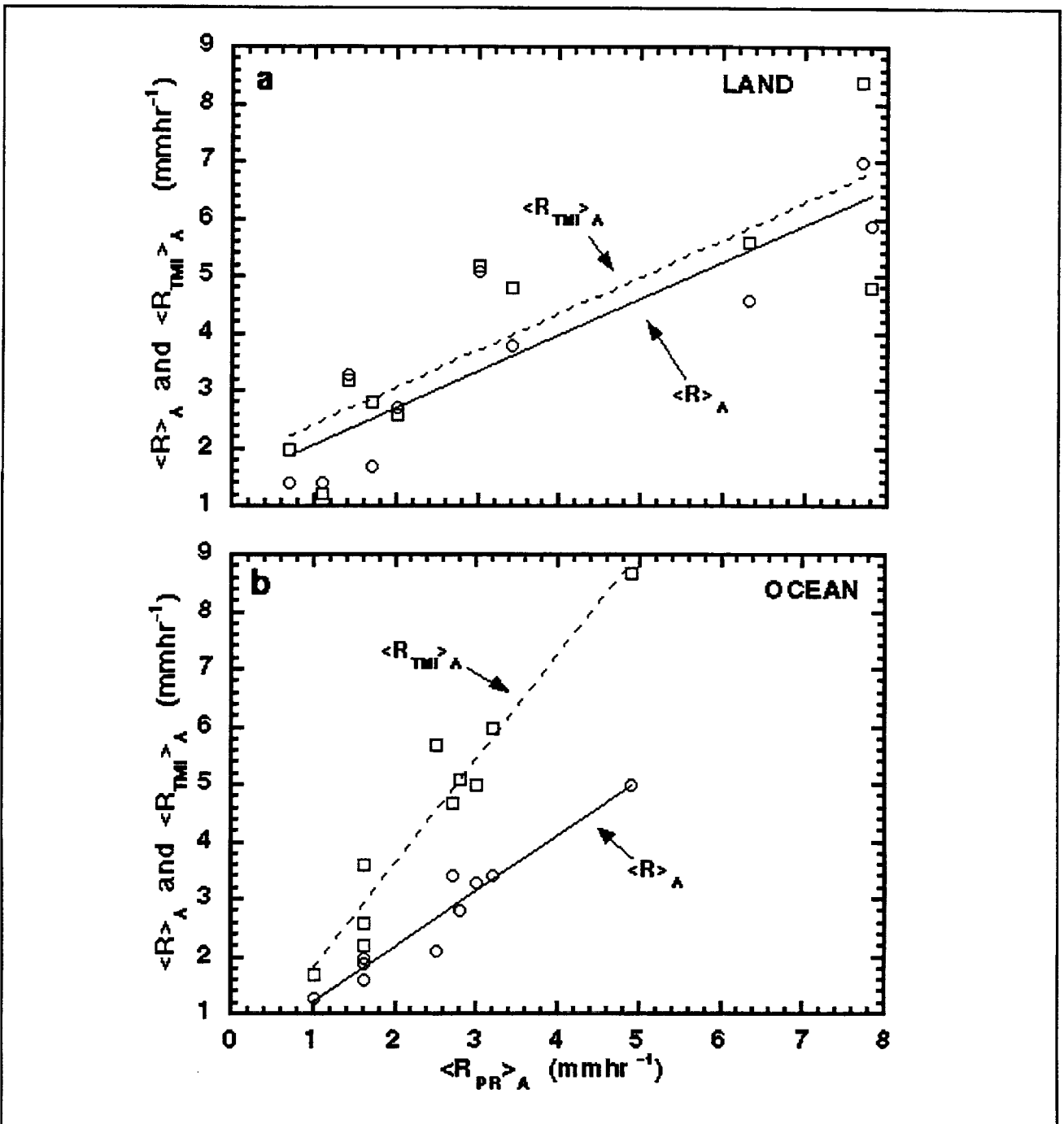
Figure 7. a) Scatter plot of the mesoscale area-average rain rates $\langle R \rangle_A$ and $\langle R_{TMI} \rangle_A$ versus $\langle R_{PR} \rangle_A$ for the 10 rain events over land.
Corr. Coef. ($\langle R_{PR} \rangle_A$ vs. $\langle R \rangle_A$) = 0.89
Corr. Coef. ($\langle R_{PR} \rangle_A$ vs. $\langle R_{TMI} \rangle_A$) = 0.84
b) Scatter plot similar to figure 7a for the 10 rain events over ocean.
Corr. Coef. ($\langle R_{PR} \rangle_A$ vs. $\langle R \rangle_A$) = 0.97
Corr. Coef. ($\langle R_{PR} \rangle_A$ vs. $\langle R_{TMI} \rangle_A$) = 0.96
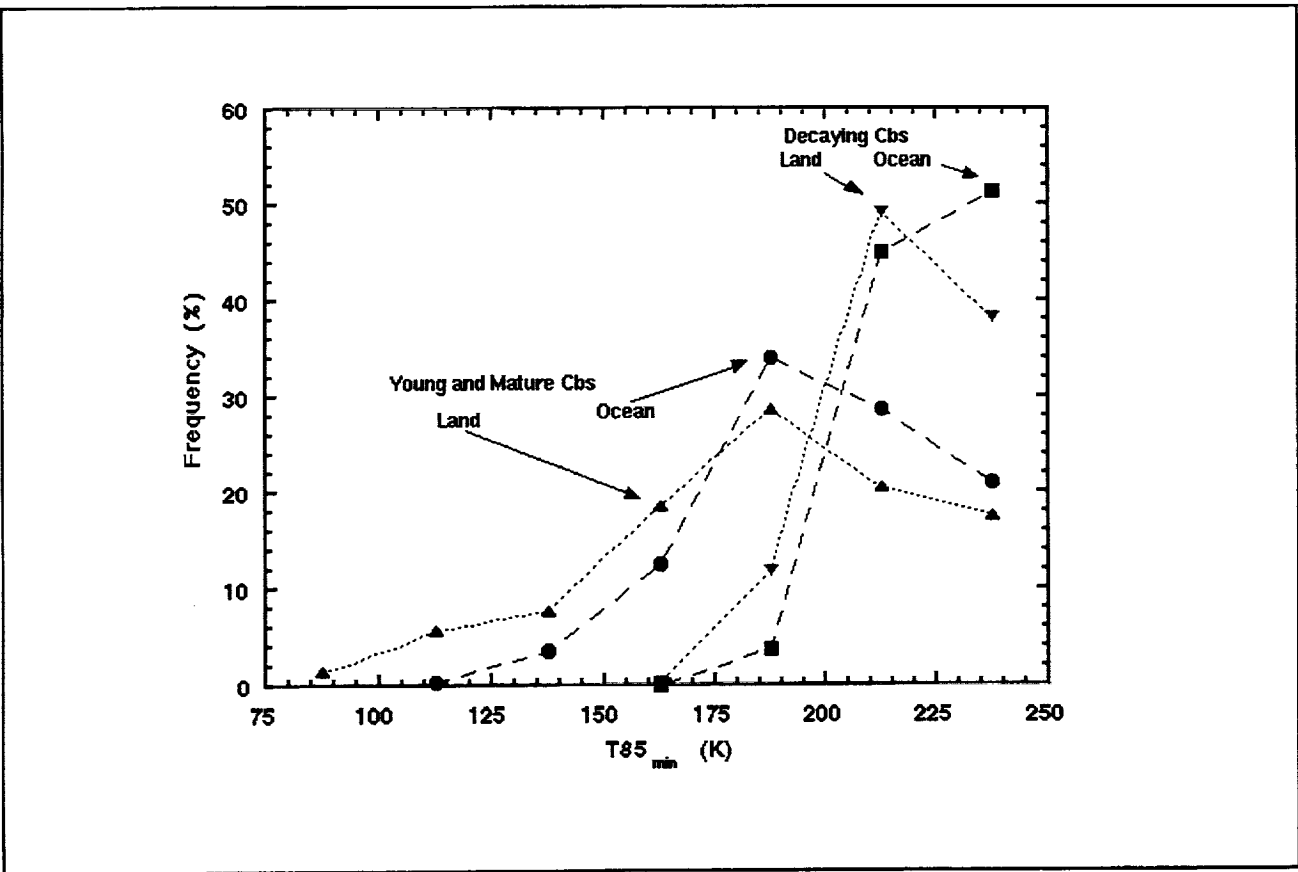
**Figure 8.** Frequency distribution of the convectively active young and mature thunderstorms, as well as the decaying thunderstorms, over land and ocean.

5. CONCLUSIONS

Multispectral, dual-polarization measurements made by satellite-borne microwave radiometers do not contain enough independent pieces of information to derive the amount and the vertical distribution of the liquid, mixed phase, and frozen hydrometeors present in the atmosphere. Without additional information, this leads to uncertainties in radiative transfer modelling and quantitative estimation of rain rate pertaining to convective and stratiform rain. In Prabhakara et al. (1998, 1999), the fractional rain area in a mesoscale region derived from the microwave radiometer is used as additional information to derive mesoscale-average rain rate. The basis for this broad relationship is contained in the dynamics of Mesoscale Convective Systems which produces rain in that area. This method, based on fractional rain area, does not identify stratiform from convective rain areas.

In the last two decades, remote sensing of rain with the help of satellite-borne microwave radiometer observations has made significant progress. At present, the spatial resolution of the Tropical Rainfall Measuring Mission (TRMM) Microwave Imager (TMI) radiometer (~ 5.5 km at 85 GHz) has improved to the point that it can readily reveal some detailed information on a scale of thunderstorms, i.e., about 20 km. This capability is needed to retrieve convective rain. In the present method, we utilize TMI radiometer data, and the conceptual framework that thunderstorm scale dynamics (~ 20 km) establishes a relationship between the spatial distribution of T85 and the existence of Cbs of different types: *young, mature, and decaying.* An important result of this study is that discrimination of convectively active young and mature Cbs from the stratiform or decaying Cbs can be done objectively. Also, we take into consideration radiative transfer properties associated with the hydrometeors of these three different categories of Cbs and infer relationships between the rain rate in these Cbs and $T85_{min}$. Initially, the rain rate observations made by the TRMM PR are

used to tune these relationships. This entire procedure constitutes the basis for separation of convective rain from stratiform rain.

Results produced from independent rain events over land and ocean show a good consistency between our method and the PR. As a consequence of this capabilitiy, we can extend the rain information given by the 220 km swath of radar to the full 760 km swath of the TMI. Also, since we are able to get a fair separation of the convective and the stratiform rain on a wider swath, it could help to determine the latent heat input into the atmosphere over a larger area and contribute to improvements in the performance of general circulation models. The method developed here is computationally simple and fast, and can be used as an effective tool to generate the climatology of precipitation over the tropics.

We may bring to the attention of the reader some inherent limitations in the present rain retrieval method. We are assuming that all Cbs, regardless of their type, have a scale of 20 km on the average, and that they have a circular shape. These assumptions may not be valid. The strong updrafts in the Cbs may be tilted (e.g., Houze, 1993 figure 9.20c) as observed by dual-Doppler radars. This leads to a given T85 minimum that does not collocate with the actual center of the Cb. The present algorithm has the ability to retrieve rain in relatively warm cloud cells of young Cbs that have sufficient vertical growth to produce some ice. However, light rain associated with boundary layer stratocumulous clouds in the tropical regions will not be detected in our algorithm. The actively developing and decaying portions of a Cb that may be close together (Houze, 1997) are not resolved in the present method. These limitations will lead to some errors in the retrieved rain rate. Improvement in the spatial resolution of the microwave radiometer, and better methods to identify different kinds of hydrometeors, will be helpful in advancing the remote sensing capability.

The key aspect of this analysis is that it recognizes textural information in space contained in the brightness temperature measurements. Based on two parameters derived from this texture information, convective versus stratiform rain discrimination is done. In two rain retrieval studies by Hong et al. (1999) and Olson et al. (1999), some textural information is also used. However, our application of the texture information differs with respect to these studies in three significant ways. First, they use this texture information to derive convective/stratiform fraction on a footprint scale, i.e., the Convective/ Stratiform Index (CSI). In our method, the texture information allows us to determine on a scale of thunderstorms (~ 20 km) the presence of actively growing convective Cbs and decaying stratiform Cbs, as well as stratiform rain where there are no Cbs. Second, in the stratiform region, we contend that the melting layer, together with the ice-aggregates above that layer, can produce cold brightness temperatures in the 85 GHz that are as low as 200 K. In the studies of Hong et al. and Olson et al., importance is not given to this melting layer mechanism in estimating CSI. Finally, our scheme is applicable equally well on land and ocean, while those of Hong et al. and Olson et al. are not. Following the rain retrieval scheme that we have developed, we do not find significant biases with respect to the radar rain observations. However, Olson et al. (1999) comment that the two other rain retrieval methods mentioned above tend to produce a high bias.

REFERENCES

Battan, L.J., 1973: *Radar Observations of the Atmosphere*. The University of Chicago Press, 324 pp.

Conner, M.D., and G.W. Petty, 1998: Validation and intercomparison of SSM/I rain-rate retrieval methods over the continental United States. *J. Appl. Met.*, **37**, 679–700.

Doneaud, A.A., S. Ionescu-Niscov, D.L. Priegnitz, and P.L. Smith, 1984: The Area Time Integral as an indicator for convective rain volume. *J. Clim. Appl. Met.*, **23** , 555–561.

Heymsfield, G.M., I.J. Caylor, J.M. Shepherd, W.S. Olson, S.W. Bidwell, W.C. Boncyk, and S. Ameen. 1996: Structure of Florida thunderstorms using high-altitude aircraft radiometer and radar observations. *J. Appl. Met.*, **35**, 1736–1762.

Hollinger, J., R.C. Lo, G. Poe, R. Savage, and J. Pierce, 1987: *Special Sensor Microwave Imager Guide*. Naval Research Laboratory, Washington, D.C., 120 pp.

Hong, Y., C.D. Kummerow, and W.S. Olson, 1999: Separation of convective and stratiform precipitation using microwave brightness temperature. *J. Appl. Met.*, **38**, in press.

Houze Jr., R.A. and A.K. Betts, 1981: Convection in GATE. *Rev. Geophys. and Space Phys.*, **41**, 541–576.

Houze Jr., R.A., 1993: *Cloud Dynamics*. Academic Press, Inc., San Diego, 571 pp.

Houze Jr., R.A., 1997: Stratiform precipitation in regions of convection: A meteorological paradox? *Bull. Amer. Met. Soc.*, **78**, 2179–2196.

Jones, D.M.A. and A.L. Sims, 1978: Climatology of instantaneous rainfall rates. *J. Appl. Met.*, **17**, pp. 1135–1140.

Kummerow, C., R.A. Mack, and I.M. Hakkarinen, 1989: A self-consistency approach to improved microwave rainfall estimation from space. *J. Appl. Met.*, **28**, 869–884.

Kummerow, C., 1998: Beamfilling errors in passive microwave rainfall retrievals. *J. Appl. Met.*, **37**, 356–370.

Lopez, R.E., D. Atlas, D. Rosenfeld, J.L. Thomas, D.O. Blanchard, and R.L. Holle, 1989: Estimation of rainfall using the Radar Echo Area Time Integral. *J. Appl. Met.*, **28**, 1162–1175.

McGhaughey, G. and E. Zipser, 1996: Passive microwave observations of the stratiform regions of two tropical oceanic Mesoscale Convective Systems. *J. Appl. Met.*, **35**, 1949–1962.

Oki, R., A. Sumi, D.A. Short, 1997: Sampling simulation of TRMM rainfall estimation using Radar-AMeDAS composites. *J. Appl. Met.*, **36**, 1480–1492.

Olson, W.S., C. Kummerow, G.M. Heymsfield, and L. Giglio, 1996: A method for combined passive-active microwave retrievals of cloud and precipitation profiles. *J. Appl. Met.*, **35**, 1763–1789.

Olson, W.S., C. Kummerow, Y. Hong, and W.-K. Tao, 1999: Atmospheric latent heating distributions in the tropics derived from satellite passive microwave radiometer measurements. *J. Appl. Met.*, **38**, 633–664.

Prabhakara, C., G. Dalu, G.L. Liberti, J.J. Nucciarone, and R. Suhasini, 1992: Rainfall over oceans: Remote sensing from satellite microwave radiometers. *Met. and Atmos. Phys.*, **47**, 177–199.

Prabhakara C., J.J. Nucciarone, and J.-M. Yoo, 1995: Examination of global atmospheric temperature monitoring with satellite microwave measurements 1) Theoretical consideration. *Climatic Change*, **30**, 349–366.

Prabhakara, C., R. Iacovazzi Jr., R. Meneghini, R. Oki, D.A. Short, M. Cadeddu, and J.A. Weinman, 1998: A TRMM microwave radiometer rain retrieval technique based on fractional rain area, *J. Met. Soc. Japan*, **76**, 765–781.

Prabhakara, C., R. Iacovazzi Jr., R. Oki, J.A. Weinman, 1999: A microwave radiometer rain retrieval method applicable to land areas, *J. Met. Soc. Japan*, in press.

Schols, J.L., J.A. Weinman, R.E. Stewart, and R.P. Lawson, 1995: The retrieval of dry and wet snow distributions from SSM/I mea-

surements and MM5 forecast results. *Proceedings of International Geosciences and Remote Sensing Symposium*. IGARSS'95.

Schols, J.L., J.A. Weinman, G.D. Alexander, R.E. Stewart, L.J. Angus, and A.C.L. Lee, 1999: Microwave properties of frozen precipitation around a North Atlantic cyclone. *J. Appl. Met.*, **38**, 29–43.

Simpson, J., C. Kummerow, W.-K. Tao, and R.F. Adler, 1996: On the tropical rainfall measuring mission (TRMM). *Met. and Atmos. Phys.*, **60**, 19–36.

Smith, E.A. and A. Mugnai, 1992: Foundations for statistical-physical precipitation retrieval from passive microwave satellite measurements. Part 1: Brightness temperature properties of a time-dependent cloud radiation model. *J. Appl. Met.*, **31**, 532–552.

Steiner, M., R.A. Houze, and S.E. Yuter, 1995: Climatological characterization of three-dimensional storm structure from operational radar and rain gauge data. *J. Appl. Met.*, **34**, 1978–2007.

Tokay, A., and D.A. Short, 1996: Evidence from tropical raindrop spectra of the origin of rain from stratiform versus convective clouds. *J. Appl. Met.*, **35**, 355–371.

Wu, R. and J.A. Weinman, 1984: Microwave radiances from precipitating clouds containing aspherical ice, combined phase, and liquid hydrometeors. *J. Geophy. Res.*, **89**, 7170–7178.

APPENDIX

REDUNDANCY IN THE MICROWAVE RADIOMETER DATA

The microwave radiative transfer formalism neglecting mixed phase hydrometeors has been developed in several studies (e.g., Wu and Weinman, 1984; Kummerow et al., 1989; Smith and Mugnai, 1992; and Prabhakara et al., 1995). These simulations form the basis for the theoretical estimation of rain rate when mixed phase hydrometeors are neglected. In these studies, the ice hydrometeors are treated as dense solid particles. The vertical profiles of the water and ice hydrometeors in relation to the rain rate are prescribed in some known fashion, and then the brightness temperature in each channel of the radiometer is simulated as a function of rain rate.

In the above simulations, mixed phase particles applicable to stratiform rain were not included. In a recent investigation, Schols et al. (1999) presented a radiative transfer formalism that simulates the brightness temperature in stratiform rain events. Schols et al.'s calculations include low-density ice aggregates (snow) above the freezing level and the melting layer below that level, which is composed of slowly descending particles. They show that the melting layer enhances significantly the emission of microwave radiation in all the channels of the radiometer (19, 37, and 85 GHz). At the same time, they indicate that for a given rain rate the scattering of radiation in the 85 GHz channel by the low-density snow particles present above the melting layer is weaker than that due to solid ice particles.

In order to assess the amount and vertical distribution of these hydrometeors, microwave radiometers (SSM/I and TMI) are configured with several spectral channels that differ significantly in their ice and water extinction properties. However, because of redundancy in the response of these multispectral dual polarization channels of the radiometer to various hydrometeors (e.g.,

Prabhakara et al., 1992), we cannot objectively separate the information about rain from that of the other hydrometeors. In order to demonstrate the redundancy in the multichannel radiometer measurements, we show in figures A1a, A1b, and A1c, maps of the brightness temperatures in the 10, 19, and 85 GHz horizontal polarization channels over a region of the Western Pacific Ocean for a rain event that occurred on 7 January 1999. A map of PR rain rate corresponding to this event is shown in figure A1d. From these figures, we observe that the brightness temperatures in the long-wavelength channels at 10 and 19 GHz show warming that corresponds to heavy convective rain, as well as light stratiform rain. In the case of the short wavelength 85 GHz channel, both convective and stratiform rain show a decrease in brightness due to scattering in these same regions. Thus, the strong convective rain cannot be easily discriminated from the weak stratiform rain with the help of 10, 19, and 85 GHz measurements.

To elucidate this redundancy more vividly, in figure A2 we show a scatterplot of T10 versus T85 deduced from several ocean rain events. The T85 data presented in this figure have been degraded to a resolution of about 35 km to correspond to that of the 10 GHz data. The negative correlation between these two data sets is about 0.72. The negative correlation arises because of scattering effects in 85 GHz, and corresponding emission effects in 10 GHz. These two channels represent the spectral extrema of the TMI. The other long-wavelength channels of this instrument at 19, 22, and 37 GHz bear similar comparison to T85, which emphasizes the redundancy in the spectral data.

TMI AND PR DATA FOR 7 JAN 99
OVER OCEAN
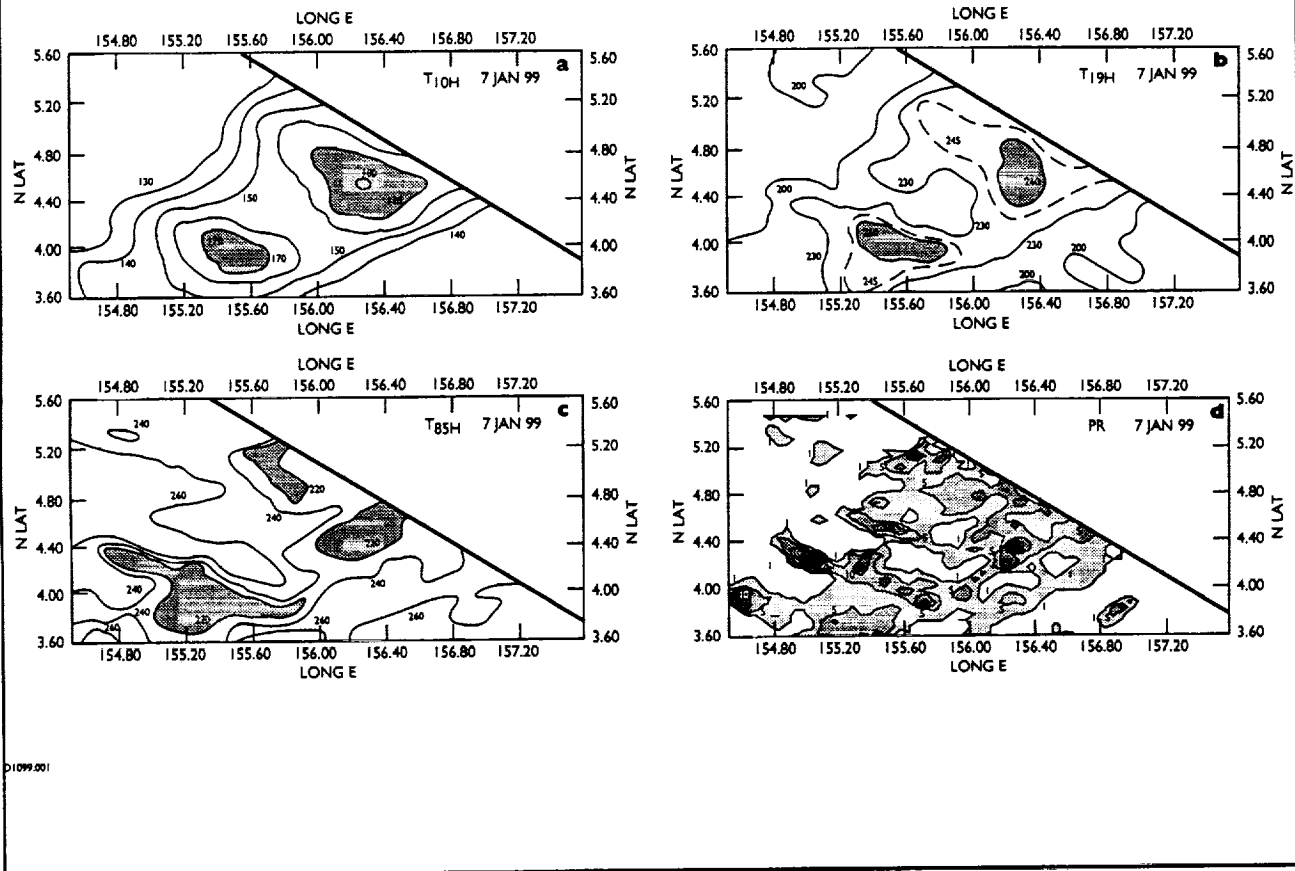
Figure A1. Maps of the data for a rain event of 7 January 1999 over the Western Tropical Pacific Ocean near 5° N and 156° E.
a) TMI measured 10 GHz brightness temperature in the horizontal polarization.
b) TMI measured 19 GHz brightness temperature in the horizontal polarization.
c) TMI measured 85 GHz brightness temperature in the horizontal polarization.
d) PR rain rate corresponding to this event.
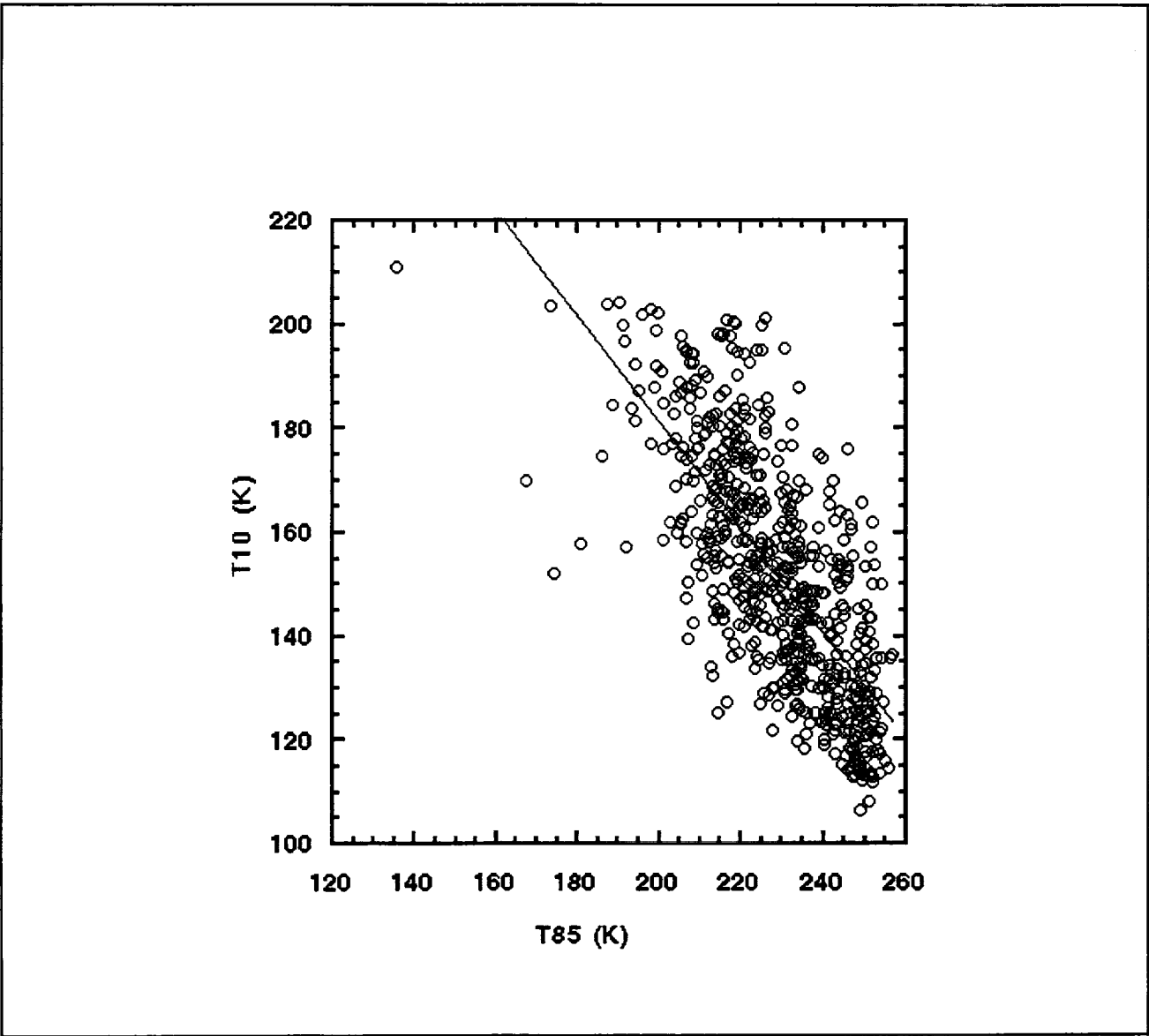
Figure A2. Scatterplot of T10 versus T85 in the horizontal polariza-
tion deduced from several ocean rain events. The T85 data presented
in this figure have been degraded to a resolution of about 35 km to
correspond to that of the 10 GHz data.
Corr. Coeff. = 0.72.

REPORT DOCUMENTATION PAGE

Public reporting burden for this collection of information is estimated to average 1 hour per response, including the time for reviewing instructions, searching existing data sources, gathering and maintaining the data needed, and completing and reviewing the collection of information. Send comments regarding this burden estimate or any other aspect of this collection of information, including suggestions for reducing this burden, to Washington Headquarters Services, Directorate for Information Operations and Reports, 1215 Jefferson Davis Highway, Suite 1204, Arlington, VA 22202-4302, and to the Office of Management and Budget, Paperwork Reduction Project (0704-0188), Washington, DC 20503.

1. AGENCY USE ONLY (Leave blank)	2. REPORT DATE	3. REPORT TYPE AND DATES COVERED
	September 1999	Technical memorandum

4. TITLE AND SUBTITLE

TMI Rain Rate Estimation Over Land and Ocean Utilizing Convective and Stratiform Discrimination

5. FUNDING NUMBERS

913

6. AUTHOR(S)

C. Prabhakara, R. Iacovazzi Jr., J.A. Weinman, and G. Dalu

7. PERFORMING ORGANIZATION NAME(S) AND ADDRESS (ES)

Climate and Radiation Branch
Laboratory for Atmospheres
Goddard Space Flight Center
Greenbelt, Maryland 20771

8. PEFORMING ORGANIZATION REPORT NUMBER

99B00076

9. SPONSORING / MONITORING AGENCY NAME(S) AND ADDRESS (ES)

National Aeronautics and Space Administration
Washington, DC 20546-0001

10. SPONSORING / MONITORING AGENCY REPORT NUMBER

TM—1999–209479

11. SUPPLEMENTARY NOTES

Iacovazzi: Raytheon ITSS Corp.
Dalu: CNR

12a. DISTRIBUTION / AVAILABILITY STATEMENT

Unclassified–Unlimited
Subject Category: 47
Report available from the NASA Center for AeroSpace Information,
7121 Standard Drive, Hanover, MD 21076-1320. (301) 621-0390.

12b. DISTRIBUTION CODE

13. ABSTRACT (Maximum 200 words)

Tropical Rainfall Measuring Mission (TRMM) Microwave Imager (TMI) radiometer brightness temperature data in the 85 GHz channel (T85) reveal distinct local minima in a regional map containing a Mesoscale Convective System (MCS). This is because of relatively small footprint size (~ 5.5 km) and strong extinction properties in this channel of the TMI. A map of rain rate for that region, deduced from simultaneous measurements made by the Precipitation Radar (PR) on board the TRMM satellite, reveals that these T85 minima, produced by scattering, correspond to local PR rain maxima. Utilizing the PR rain rate map as a guide, we infer from TMI data the presence of three different kinds of thunderstorms or Cbs. They are young, mature, and decaying Cbs that have a scale of about 20 km on the average. Two parameters enable us to infer these three kinds of Cbs objectively: a) the magnitude of scattering depression deduced from local T85 minima and b) the mean horizontal gradient of T85 around such minima. Knowing the category of a given Cb, we can estimate the rain rate associated with it. Such estimation is done with the help of relationships linking T85 minimum to rain rate in each Cb type. Similarly, a weak background rain rate in all the areas where T85 is less than 260 K is deduced with another relationship linking T85 to rain rate. In our rain retrieval model, this background rain constitutes the stratiform rain where the Cbs are absent. Initially, these relationships are optimized or tuned utilizing the PR and TMI data of a few MCS events. After such tuning, the model is applied to independent MCS cases. The areal distribution of light (1–10 mmhr^{-1}), moderate (10–20 mmhr^{-1}), and intense ($\geq$ 20 mmhr^{-1}) rain rates are retrieved satisfactorally. Accuracy in the estimates of the light, moderate and intense rain areas and the mean rain rates associated with such areas in these independent MCS cases is on the average about 15%. Taking advantage of this ability of our retrieval method, one could derive the latent heat input into the atmosphere over the 760 km wide swath of the TMI radiometer in the tropics.

14. SUBJECT TERMS

Tropical Rainfall Measuring Mission (TRMM) Microwave Imager (TMI); Mesoscale Convective System (MCS); remote sensing.

15. NUMBER OF PAGES

27

16. PRICE CODE

17. SECURITY CLASSIFICATION OF REPORT	18. SECURITY CLASSIFICATION OF THIS PAGE	19. SECURITY CLASSIFICATION OF ABSTRACT	20. LIMITATION OF ABSTRACT
Unclassified	Unclassified	Unclassified	UL